Critical exponents of the superconducting transition in granular $YBa_2Cu_3O_{7-\delta}$

R. J. Joshi and R. B. Hallock
Laboratory for Low Temperature Physics, Department of Physics and Astronomy, University of Massachusetts, Amherst, Massachusetts 01003

J. A. Taylor
New York State College of Ceramics, Alfred University, 2 Pine Street, Alfred, New York 14802
(Received 12 September 1996)

We present the results of measurements designed to study superconducting I-V scaling in samples of polycrystalline $YBa_2Cu_3O_{7-\delta}$ with varying mean grain sizes, $1\ \mu m \leq \langle d_g \rangle \leq 20\ \mu m$ at selected magnetic fields, $0.5\ G \leq H \leq 10$ T. I-V isotherm measurements performed near the superconducting transition on the samples are consistent with recent predictions of I-V scaling, with critical exponents $\nu \sim 1.1-1.75$ and $z \sim 2.3-4.3$. The values for ν are comparable to those previously reported. The values for z are somewhat lower than what is predicted by the glassy models. The static exponent ν does not display any grain-size or magnetic-field dependence. The dynamic exponent, however, does display some morphology dependence with z higher for the small grain-size samples. The data shows some evidence for a crossover between low and high z values in increasing magnetic fields. [S0163-1829(97)06213-9]

INTRODUCTION

Granular high-T_c materials, with their extremely short coherence lengths, weak intergranular coupling, and high transition temperatures provide an experimental realization of the Josephson array model.[1] However, these materials also contain a high degree of disorder and randomness with regard to the grain sizes, positions, and coupling strengths. Thus, given their considerable complexity it is unclear whether these systems should undergo a phase transition into a superconducting state. Early experimental studies on polycrystalline $YBa_2Cu_3O_{7-\delta}$ (YBCO) showed power-law behavior in the transport characteristics as well as a characteristic two-stage resistive transition.[2] Later it was shown that power law I-V characteristics could be predicted using the gauge glass model.[3,4] Motivated by the experimental results, Fisher, Fisher, and Huse proposed the existence of an additional state in the superconductors, the vortex glass.[5,6] Most transport measurements done on bulk YBCO are restricted to the low-,[7] intermediate-,[8] or high[8]-field regions. Although some of these studies have been done on samples of varying morphologies, the range in grain sizes is fairly narrow. These studies report several different values for the critical exponents[7,8] ν and z suggesting that the exponents in these systems may be field and morphology dependent. In this work we explore both these issues by taking extensive sets of transport measurements over five decades in magnetic field, $0.5\ G < H < 10$ T, and on several samples with mean grain sizes ranging from 1 to 20 μm. Our experimental envelope for the I-V data was chosen so as to optimize sensitivity to the critical region (within instrumentation limits) and also to be comparable to that used by other groups.[8] The data was taken over four decades in current density, $0.1\ mA/cm^2 < J < 1\ A/cm^2$, and six decades in electric field, with minimum sensitivity of 2 nV/cm.

GRANULAR SUPERCONDUCTIVITY

The early studies of granular superconductivity were focused on two types of systems: granular materials and fabricated Josephson-junction arrays. These systems display a characteristic two-stage resistive transition as they are cooled. The first stage is associated with the onset of superconductivity in the grains and the second stage is indicative of intergranular coupling. The intergranular coupling is best modeled as a superconductor-normal-superconductor Josephson junction.[9] The Josephson effect predicts the flow of a resistanceless current across the junction for currents below a certain critical value. In the absence of magnetic field the Josephson equations can be expressed as

$$I_J = I_J^0 \sin(\theta_i - \theta_j), \tag{1}$$

$$V_{ij} = (h/2\pi e)\, d(\theta_i - \theta_j)/dt, \tag{2}$$

$$E_J = -(h/2\pi e) I_J^0 \cos(\theta_i - \theta_j), \tag{3}$$

where I_J, V_{ij}, and E_J are the Josephson current across the junction, voltage across the junction, and the Josephson coupling energy, respectively. θ_i and θ_j are the phases of the superconducting order parameter in adjacent grains. I_J^0 is the Josephson critical current, which is the maximum current that can pass through the junction without dissipation. The temperature dependence of I_J, V_{ij}, and E_J enters via the critical current, I_J^0 as

$$I_J^0 = (\pi\Delta/2eR_n)\tanh(\Delta/2k_BT), \tag{4}$$

where Δ is the BCS gap parameter and R_n is the junction resistance.[10] From this equation we see that the critical current and hence the coupling energy increases as the temperature is lowered. Above the superconducting transition thermal fluctuations scramble the phase coherence across the junctions and a voltage appears across the junction in accor-

dance with Eq. (2). With decreasing temperature the coupling energy E_J becomes strong enough to overcome the thermal fluctuations k_BT, producing a transition into a state of zero resistivity. Under these conditions the first two Josephson equations predict a nonzero superconducting current. Numerical simulations of the effects of thermal fluctuations on the I-V characteristics of a Josephson junction have been performed by Ambegaokar and Halperin.[11] They found that the I-V characteristics were Ohmic at high temperatures, highly nonlinear at lower temperatures, and superconducting as $T\rightarrow 0$.

The application of a magnetic field to a Josephson-junction array introduces an additional term in the phase difference across adjacent grains. This term is just the line integral of the vector potential across the junction and is given by

$$A_{ij}=(2\pi/\phi_0)\int \mathbf{A}\cdot\mathbf{dl}. \tag{5}$$

Thus the expressions for the Josephson current and Josephson energy become

$$I_J=I_J^0\sin(\theta_i-\theta_j+A_{ij}), \tag{6}$$

$$E_J=-(h/2\pi e)I_J^0\cos(\theta_i-\theta_j+A_{ij}). \tag{7}$$

The model Hamiltonian for the granular array is then given by

$$H=-(h/2\pi e)\sum_{(i,j)} I_{ij}^0\cos(\theta_i-\theta_j+A_{ij}). \tag{8}$$

In a disordered Josephson array the individual I_{ij}^0 have different magnitudes but keep the same sign. This is in contrast with a spin glass where the coupling energies can vary both in magnitude and in sign. For the disordered Josephson array frustration is introduced via the vector potential term. In granular samples with random grain sizes and positions the flux threading individual junctions will vary considerably. This means that the A_{ij} will vary over its entire accessible range $[0,2\pi]$, thus permitting sign reversals in the coupling energy and hence leading to strong frustration between the individual phases. Frustration destroys the long-range order in the phases that was present in the zero-field Meissner (ferromagnetic) phase. This, however, does not mean that the individual phases cannot freeze into a sample specific glassy configuration. Since the glassiness in this system was introduced via the vector potential, this state has been called the gauge glass.[3,4] This transition from a ferromagnetic to a glassy state was found to occur above a characteristic glass field[3] given by $H_g\sim\phi_0/2\xi_p^2$, where ξ_p is the percolation coherence length. For a granular sample $\xi_p\sim\langle d_g\rangle$, the average grain size in the sample. At the glass field there is approximately half a flux quantum per granular cross section. For typical granular samples $H_g<1$ G. For fields below H_g, the granularity of the medium is no longer important and the system can be analyzed in terms of a set of averaged ''effective-medium'' parameters.[9]

One way of searching for a phase transition into the glassy state is via the Fisher, Fisher, and Huse (FFH) critical scaling hypothesis.[5] This hypothesis was originally motivated by I-V isotherm measurements performed by Koch *et al.*[12] on thin-film samples of YBCO. For YBCO samples with strong enough random pinning, the transition is expected to be of second order and hence should be describable by critical scaling behavior near the transition. A second-order phase transition is associated with the development of long-range correlations that can be described in terms of a power divergence in the coherence length in the vicinity of the transition:

$$\xi\sim|\vartheta|^{\nu}, \tag{9}$$

where $\vartheta=(T-T_c)/T_c$ is the reduced temperature and ν is the static exponent. The divergence in the superconducting electron density for a d-dimensional system is given by

$$n_s\sim|\psi|^2\sim\xi^{d-2}. \tag{10}$$

Like spin glasses, the vortex glass is an example of a dynamic critical phenomena. The dynamic properties of these systems can be described via a power-law divergence in the characteristic relaxation times, τ; with

$$\tau\sim\xi^z\sim|\vartheta|^{\nu z}, \tag{11}$$

where z is the dynamic critical exponent. τ is the time scale associated with the relaxation of a fluctuation of size ξ.

The assumptions about the static and dynamic properties of the system can be incorporated into a single expression that predicts the I-V response of the system in the critical region. This equation is known as the FFH scaling form and is given by

$$E\sim J\xi^{d-2-z}\epsilon_{\pm}(J/J_0), \tag{12}$$

where E is the electric field, J is the current density, and $\epsilon_{\pm}$ are the universal scaling curves above and below T_c. J_0 is a characteristic current density that separates the low J thermally activated dissipative regime from the high J current-driven dissipative regime. Scaling arguments can be invoked to predict the power-law divergence of J_0,

$$J_0\sim\xi^{-(d-1)}. \tag{13}$$

Using Eqs. (10)–(12) we can rewrite the scaling form in terms of the coherence length as

$$E\sim J|\vartheta|^{\mu}\epsilon_{\pm}(J/|\vartheta|^{\lambda}), \tag{14}$$

where μ and λ are experimentally accessible critical exponents and are given by

$$\mu=\nu(z+2-d), \tag{15}$$

$$\lambda=\nu(d-1). \tag{16}$$

Hence, an experimental analysis using the FFH scaling form in the critical region can be used to extract the more fundamental critical exponents ν and z. For a three-dimensional (3D) system

$$\nu=\lambda/2, \tag{17}$$

$$z=1+2\mu/\lambda. \tag{18}$$

We now consider the consequences of the scaling hypothesis on the I-V isotherm measurements. Above T_c the E-J curves are Ohmic over the entire range in J. Between the temperature corresponding to Ohmic behavior and the transition temperature T_c, the isotherms display a crossover from Ohmic to power-law behavior. This crossover from Ohmic to power-law behavior can be expressed via a crossover current density J_x^+, where

$$J_x^+ \sim |\vartheta|^{\lambda}. \tag{19}$$

The Ohmic portion is predicted to have the power-law dependence,

$$\rho_L \sim |\vartheta|^{\mu}. \tag{20}$$

This provides a consistency check on the exponent μ. At T_c the diverging correlation length must cancel out so as to keep E finite. Using Eqs. (12) and (13) this means that $\epsilon_{\pm}(J/\xi^{-(d-1)}) \sim (J/\xi^{-(d-1)})^{\alpha} = \xi^{d-2-z}$, thus implying that

$$E \sim J^a, \quad \text{at } T = T_c, \tag{21}$$

where

$$a = 1 + \alpha, \quad \alpha = (d + z - 2)/(d - 1). \tag{22}$$

Thus right at the transition the I-V characteristic reduces to a power law, with power-law exponent a. Below T_c the response is glassy at large length scales (small current densities) and power law at short length scales (high J). The crossover from glassy to power-law behavior can be expressed via a crossover current density J_x^-, where

$$J_x^- \sim |\vartheta|^{\mu}. \tag{23}$$

The glassy response below the transition can be expressed as

$$E/J \sim \exp\{-(J_c/J)^s\}. \tag{24}$$

The exponent s directly probes the nature of the low-temperature phase. In the vortex glass theory $s \ll 1$. Dekker, Eidelloth, and Koch[13] have measured the exponent s in the low-temperature phase of granular YBCO films. They find $s \sim 0.2$ for low J and $s \sim 0.95$ at higher J providing direct evidence that the superconducting phase is a vortex glass.

Equation (14) can be recast in terms of the resistivity $\rho = E/J$ as

$$\rho/|\vartheta|^{\mu} \sim \epsilon_{\pm}(J/|\vartheta|^{\lambda}). \tag{25}$$

This equation predicts that when the rescaled resistivity, $\rho/|\vartheta|^{\mu}$ is plotted versus the rescaled current density, $x = J/|\vartheta|^{\lambda}$ all the data should lie on two universal scaling functions ϵ_+ and ϵ_- above and below T_c, respectively.

APPARATUS AND TECHNIQUES

Two different types of cryostats were used to perform the measurements described in this paper. A 77 K immersion cryostat was used for all the low- and intermediate-field I-V's and some of the temperature-dependent resistance measurements done on the bulk YBCO samples. High-field I-V data was taken on a helium refrigeration system at the National High Magnetic Field Laboratory (NHMFL).

Figure 1 shows a schematic diagram of the 77 K cryostat. A Cu connecting rod provides thermal contact between the Cu disk and the sample block. The sample block is a 3.2 mm thick×38 mm wide×102 mm long rectangular Cu slab. The sample platform and a platinum thermometer is enclosed in a copper radiation shield thermally anchored to the sample block.

A Lakeshore model LS805 temperature controller monitored the temperature of a Lakeshore DT 470 diode thermometer attached to the 33 mm Cu disk. The proportional output voltage was applied across a 10 Ω manganin wire heater bifilarly wound around the Cu disk and attached to it with GE 7031 varnish and was able to maintain the temperature of the DT-470 diode to within approximately 20 mK which resulted in a temperature stability ~1–2 mK on the sample block. Joule heating on the sample stage during I-V measurements was small (~1 mW @100 mA) and produced negligible temperature changes on the sample block. Thermal contact between the sample and the sample block was very good and the resistive data showed no noticeable temperature hysteresis between the cooling and warming runs.

A helium refrigeration system was employed to take high-field I-V data at the NHMFL. The cryostat and attached components are shown in Fig. 2. A cernox 2512 semiconducting temperature sensor was placed in a groove in the G10 holder. The sensor was thermally anchored to the rest of the assembly by a thin copper disk placed directly above it. Helium exchange gas in the vacuum insert provided the thermal link between the helium bath and the cryostat (and thus to the sample). The cooling power was adjusted by varying the exchange gas pressure.

Two types of transport measurements were performed on the samples: resistivity vs temperature and I-V isotherms. In both techniques a current I was passed through the sample and the sample voltage, V, was measured. The Ohmic resistance is given by $R = V/I$. These geometry-dependent measurements were then converted into the intrinsic quantities of interest via the usual relationships: $\rho = E/J$, $E = V/l$, $J = I/A$, $\rho = RA/l$. Here E is the electric field and J is the current density. The relevant geometric parameters are l and A, the sample length and area of cross section, respectively. The resistivity ρ was the fundamental quantity of interest extracted from the transport measurements. Low resistance contacts were made using a technique similar to that described by Ekin and co-workers[14,15] in which silver pads ~2 μm thick were evaporated on the samples. The samples were then annealed in flowing oxygen.

Our transport measurements were designed to probe the dc response of the sintered samples in the vicinity of the superconducting transition. Most of the interesting behavior occurs at very low current densities and small electric fields. In order to achieve this level of sensitivity in our measurements we adopted both dc and low-frequency phase sensitive ac techniques. For the ac measurements, sample current was a 15 Hz square wave provided by a HP 3425 synthesized function generator. The sample voltage was amplified and filtered by an ITHACO 1201 low-noise amplifier and then measured by a SR 530 lock-in amplifier via a computer. Sample current was determined by measuring the voltage

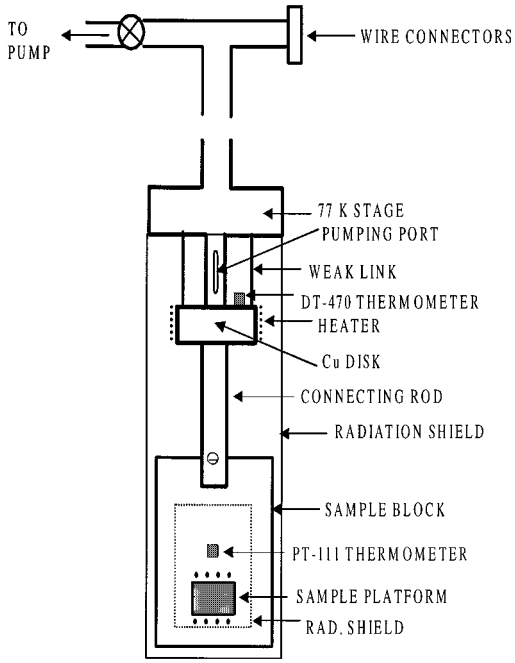

FIG. 1. 77 K cryostat.

across a precision 0.9988 Ω resistor with a PAR 129 lock-in amplifier. The output of the PAR 129 lock-in was connected to an HP 3478 multimeter so that the current could be computed. The results between the ac and dc techniques differed by a constant calibration factor of ~1.3, independent of sample current. When using the dc technique, a reversing switch was added to eliminate thermoelectric voltages. We adopted an identical protocol and technique for the high-field data acquisition performed at the NHMFL.

$\rho(T)$ and I-V data were taken over five decades in magnetic field: 0.5 G$\leqslant H\leqslant$15 T. Low to intermediate field (0.5–5000 G) runs were performed using a Varian electromagnet, model V 3603 12″ magnet connected to a V-FR2501 regulated power supply capable of producing fields 0.1 G$\leqslant H\leqslant 10^4$ G. Magnetic field was measured with a Walker Scientific model MG-50 Hall effect gaussmeter, with a range of $0.1–10^4$ G. Using this gaussmeter the vertical component between the pole pieces was measured to be less than 0.1 G. The ambient magnetic field was measured to have a magnitude $H=0.5$ G making an angle ~15° with respect to the local vertical.

High-field data was taken using a 15 T 1″ bore solenoidal Oxford superconducting magnet system S 15.45.13. The homogeneity at the magnet center was 1 part in 10^3 over 10 mm. The magnetic field/current ratio was 0.1948 T/A and typical ramp rates were ~0.2 to 2 A/min. This corresponded to 0–15 T ramp times of around 1.5 h. The field decay in persistent mode was less than 1 part in 10^4 per hour. High-field $\rho(T)$ and I-V data were taken over 1 decade in magnetic field: 1 T$\leqslant H\leqslant$15 T. Low-field check runs were also performed in the remnant central magnetic field (<50 G) of the magnet.

SAMPLE PREPARATION AND CHARACTERIZATION

The samples used for the measurements described in this paper were fabricated from two kinds of precursor

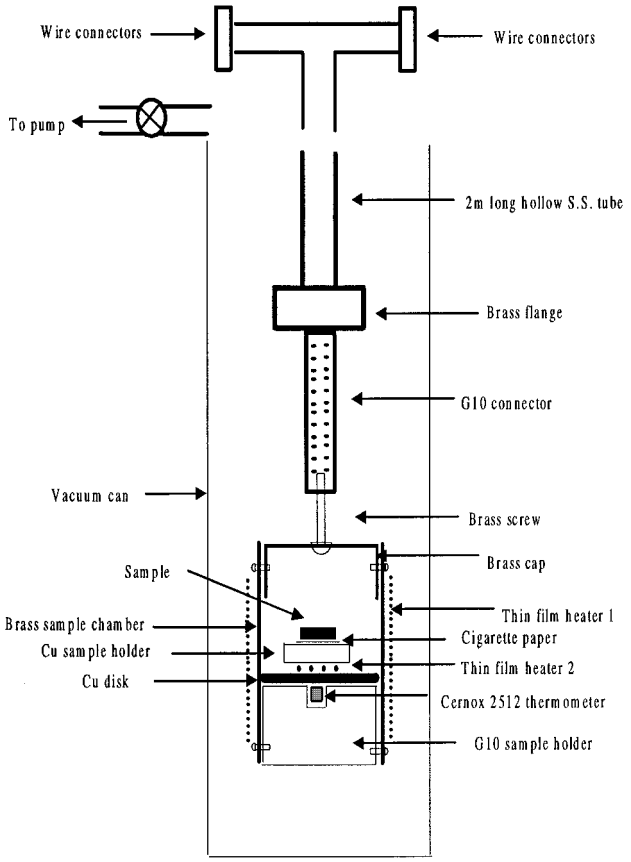

FIG. 2. High-field He_4 cryostat.

$YBa_2Cu_3O_{7-\delta}$ powders: commercially available 123 powder from Seattle Speciality Ceramics (SSC) and powder made using the standard solid-state reaction technique.[16] Powders from SSC were made using the spray pyrolysis technique.[17]

The coarse powder from the standard solid-state reaction technique was divided into two batches: one stored in a desiccator at room temperature and the other in an oven maintained at 100 °C to avoid any degradation of the 123 phase in the presence of humidity. These batches will be referred to as coarse-wet (CW) and coarse-dry (CD), respectively.

The SSC powder received no special treatment and will be referred to as SSC-fine. The three starting powders were then prepared as different particle size distributions, as described below. One fraction of the coarse-wet was separated using a 44 μm mesh screen. The powder retained on the mesh, which is called CW-V coarse, and the fraction that passed through, which is called CW-coarse, were collected separately. The CW powder was then reground in acetone with a mortar and pestle for varying times (5, 10, and 15 min). These will be referred to as CW-1, CW-2, and CW-3, respectively. X-ray-diffraction patterns of the powders before and after grinding in acetone showed them to be stoichiometrically similar to within 1–2 vol. %. An identical protocol was followed for the CD powder for grinding in acetone. Those powders will be referred to as CD-1, CD-2, and CD-3.

Processing parameters and resulting characteristics of the six samples pressed into pellets used in this paper are summarized in Table I. All six samples were subjected to a pres-

TABLE I. Processing conditions and characteristics of YBCO pellets.

Sample	*S*1	*SB*	*S*4	*S*7	*S*9	*S*15
Powder processing method	SSC	SSC	SS	SS	SS	SS
Starting powder	Dry	Dry	CW-1	CW-2	CW-1	CW-2
Initial T_{sinter} (h)			890	890	890	890
Final T_{sinter} (h)	920	940	940	940	940	940
t_{sinter} (h)	12	24	6	48	48	100
Density (g/cm^3)	5.84	5.51	5.81	5.9	5.94	5.86
ρ (96 K) (mΩ cm)	0.64	0.57	0.42	0.52	0.29	0.8
ρ (300 K) (mΩ cm)	1.34	1.23	0.86	1.1	0.62	1.74
ρ_{SG} (mΩ cm)	0.38	0.31	0.34	0.4	0.21	0.53
ρ (foot)$_{\text{onset}}$ (mΩ cm)	0.26	0.26	0.08	0.12	0.08	0.27
T_c (K)	90.75	91.1	90.4	89.3	90.4	89.5
$T(0.9\rho_n)$ (K)	93.3	93.8	92.9	91.75	92.7	92.2
$T(0.1\rho_n)$ (K)	91.5	91.65	91	89.9	91.25	90.23
$\delta T_c \equiv T(0.9\rho_n) - T(0.1\rho_n)$	1.8	2.13	1.9	1.85	1.45	1.98
$\langle d_g \rangle$ (pellet) (μm)	1.02	6.3	12.9	11.4	18.15	15.75

sure of 200 MPa in a 1.2 cm cylindrical press for initial compacting prior to firing at initial T_{sinter}. Of all the solid-state samples only those processed at the lower temperatures (initial T_{sinter}=890 °C) had reasonably narrow transitions. The samples processed at the lower temperatures were re-sintered at higher temperatures (final T_{sinter}) to facilitate further grain growth. Resistivity data for six samples is shown in Fig. 3. These curves show a two-stage superconducting transition. We were able to identify both the single grain resistivity, ρ_{SG} and the bulk superconducting temperature T_c from such measurements.

All the values listed Table I for the resistivity ρ and the density are accurate to within 5% with the uncertainty due to irregularities in the sample dimensions. To characterize the width of the superconducting transition we measure $T(0.9\rho_n)$ and $T(0.1\rho_n)$, which are the temperatures at which the resistivity has fallen to 0.9 and 0.1 of the normal-state resistivity ρ_n. ρ_n is the value of the normal-state resistivity just above the transition and is obtained from $d\rho/dT$ and ρ at 95 K. The transition width is defined as the difference between the 90% and 10% values of ρ_n. $\rho(\text{foot})_{\text{onset}}$ is defined as the value of the resistivity which shows deviations from the extrapolated single-grain part of the resistivity curve.

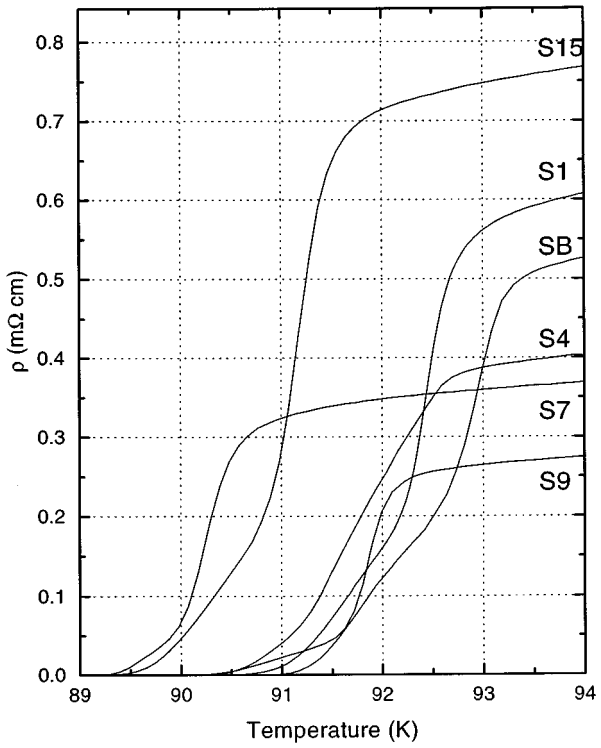

FIG. 3. ρ vs T at H=0.5 G for samples *S*1, *S*9, *SB*, *S*7, *S*15, and *S*9.

Grain-size distributions were analyzed from SEM and optical microscope images of polished sections of the samples. Polished sections were prepared by mounting fractured specimens in epoxy and then grinding and polishing one face smooth, using a series of abrasive papers followed by abrasive powders on cloth wheels. The resulting mounts were smooth to $\sim$1 μm. To resolve the grain boundaries and different phases the samples were chemically etched with 10% acetic acid. Grain-size analysis was accomplished using the linear intercept method. In this method a subset of $N_1 \sim 300$ grains were selected from the images by drawing parallel lines on the photographs. The linear dimensions of the grains intercepted by these lines were recorded as x and y. Grain sizes d_g were then calculated as the geometric mean $(xy)^{(1/2)}$ of the two dimensions. Grain-size distributions were calculated by counting the number of grains $N(d_g)$ in a 1 μm interval around integer grain sizes. The average grain size, $\langle d_g \rangle$ and the width of the distribution, δd_g, were then computed from the data. The frequency distributions $F(d_g)=N(d_g)/N_t$ for all six samples are represented by the shaded bar graphs in Fig. 4. We also noted the most probable grain size, $(d_g)_{\text{MP}}$ from the peak of the frequency distribution, $F(d_g)$.

Transport characteristics should be determined by grains occupying the largest volume fractions. The relative volume occupied by a given grain size was estimated via the volume fraction $F(V_g)=(d_g/\langle d_g \rangle)^3 F(d_g)$. Volume fraction distributions for the samples are represented by the unfilled bars in Fig. 4. Both plots show large amounts of scatter for the rela-

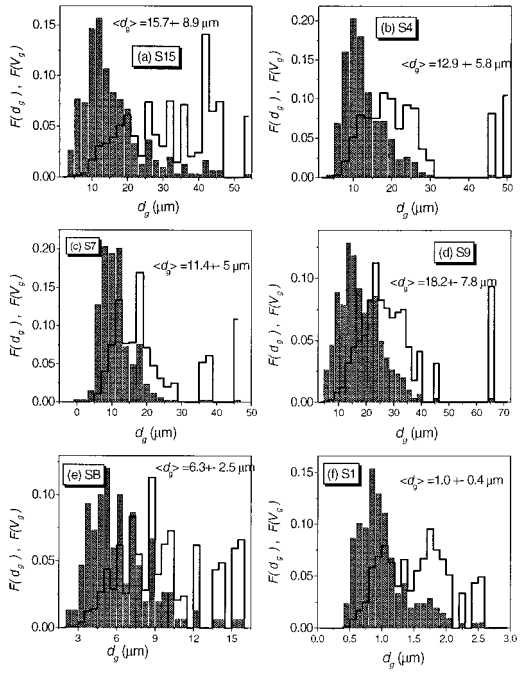

FIG. 4. Grain-size distributions for all six samples.

tively few larger grain sizes. However, comparison of the frequency distribution and volume fraction plots on the same samples show that although there are a large number of relatively small grains they occupy only a small fraction of the total volume of the sample.

In principle the samples could also be characterized via the peak in the $F(V_g)$ distribution, d_g at $F(V_g)_{\max}$. However, this is not possible since the distributions cannot be characterized by a single peak. Nevertheless, we can define a threshold grain size, $\langle d_g \rangle_V$ above which the cumulative volume fraction exceeds the percolation threshold in 3D. For a granular sample with a distribution of grain sizes the percolation fraction is 16%. Thus $\langle d_g \rangle_V$ is where $\Sigma F(V_g)=0.16$. Table II lists $\langle d_g \rangle$, δd_g, $(d_g)_{\rm MP}$, and $\langle d_g \rangle_V$ for all six samples.

Our original intent was to fabricate samples with varying grain sizes in the range 1 to 100 μm and with narrow grain-size distributions. After a considerable amount of effort we were able to produce samples with mean grain sizes in the range 1–20 μm and fairly broad grain-size distributions, with, $\langle d_g \rangle_V$ 1.5–32 μm. The absolute range in grain sizes over all six samples was 0.4–67 μm.

I-V CHARACTERISTICS OF THE SUPERCONDUCTING TRANSITION IN GRANULAR YBCO

The granular nature of our samples has important consequences on the character of the resistive transition. The resistive transitions of the six samples in selected magnetic fields and in order of increasing grain size are shown in Fig. 5. All these transitions display a sharp initial drop followed by a relatively broad foot region.

All the I-V data presented in this paper was analyzed in the context of the predictions contained within Eqs. (20), (21), and (25). Using these equations we were able to extract the values for T_c and a, μ and λ for all six samples. The static and dynamic exponents were then calculated using the relationships in Eqs. (17) and (18). We also attempted to extract λ and s from Eqs. (19) and (24). This task, however, was difficult and we were unable to obtain consistent results based on a single criterion. This was due to the restricted dynamic range, subjective nature of the respective crossover criteria and low density of data points.

A total of 36 sets of I-V isotherm measurements were performed on the six samples over five decades in magnetic field, 0.5 G$<H<$10 T. Table III summarizes the fields at which data was taken for each of the samples. In what follows we will explicitly outline the analysis steps using a representative sample, S15 at $H=100$ G.

Figure 6(a) shows E-J data for sample S15 at $H=100$ G; the same data plotted as resistivity, ρ vs J, is shown in Fig. 6(b). All the E-J data exhibit the characteristic features of a global second-order superconducting phase transition. Above T_c the E-J data is Ohmic over the entire range in J. Between the temperature corresponding to Ohmic behavior and the transition temperature T_c, the isotherms display characteristic evolution as a function of J. At high enough current densities all the isotherms display Ohmic characteristics. In intermediate J the E-J data exhibit nonlinear or power-law behavior. Finally, at low J values the isotherms develop a linear resistivity. As the temperature is lowered the region of Ohmic resistivity is reduced to lower J values. In other words, the onset of nonlinearity shifts to lower J values as the temperature approaches T_c. Finally at T_c the isotherms exhibit a power-law characteristic, $E\sim J^a$ (or $\rho\sim J^{a-1}$) for over three decades in electric field. Below T_c, it is hard to identify and distinguish between the region of critical behavior and the region of glassy behavior. However, the negative curvature of the ln$E$ vs ln$J$ isotherms is indicative of the superconducting response of the samples at these temperatures.

Analysis of the E-J isotherms close to the transition can be used to extract experimental values for T_c and the power-law exponent a. To estimate T_c we chose the isotherm that displayed the largest dynamic range of power-law behavior. The power-law exponent a was extracted from the slope of the corresponding ln$E$ vs ln$J$ isotherm. In order to estimate the precision in T_c and a we used the average deviation in temperature and slope of the neighboring $\ln E$ vs $\ln J$ isotherms. For some sets of E-J isotherms it was difficult to

TABLE II. Grain-size information for samples *S*1, *SB*, *S*4, *S*7, *S*9, and *S*15.

	*S*1	*SB*	*S*4	*S*7	*S*9	*S*15
$\langle d_g \rangle$ (μm)	1.02	6.3	12.9	11.4	18.15	15.75
δd_g (μm)	0.4	2.55	5.85	5.1	7.75	8.9
$(d_g)_{\rm MP}$ (μm)	0.85	5.3	10	10	14	12
$\langle d_g \rangle_V$ (μm)	1.54	9.7	24.35	21.8	30.1	31.9

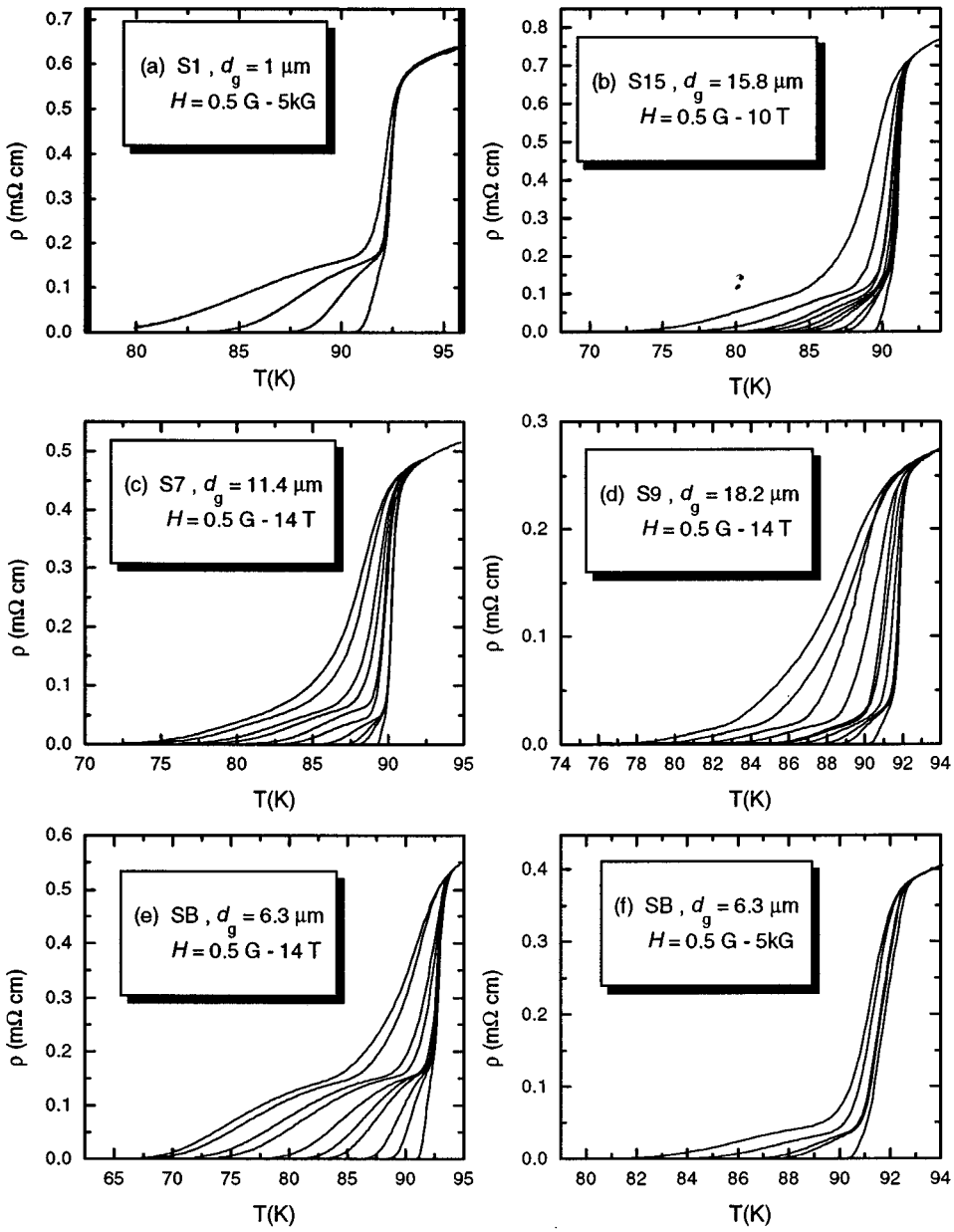

FIG. 5. ρ vs T for all six samples in selected magnetic fields.

pick out the critical isotherm. In such cases T_c and a corresponded to the average values of the temperature and the slope of the two ln$E$ vs ln$J$ isotherms with slight negative and positive curvature, respectively. Thus, for sample S15 at $H=100$ G, $T_c=87\pm0.1$, and $a=2.1\pm0.1$. In such cases the width of T_c was always less than 100 mK.

Although the procedures outlined above do provide a reasonably accurate estimate of T_c and a, they tend to overestimate both the width of the power-law behavior and the error bar for the power-law exponent. This, however, does not constitute a serious flaw in the analysis since both δT_c and δa were determined with greater precision from the data collapse.

The agreement of our E-J data with the scaling hypothesis can be tested by carrying out a data collapse. According to Eq. (25) when the rescaled resistivity is plotted vs the rescaled current density, all the data should collapse on two universal curves ϵ_+ and ϵ_-. Figure 7 shows data collapses for sample S15 at $H=100$ G. These curves show evolution in structure consistent with the scaling hypothesis. Well above T_c the isotherms are entirely Ohmic and lie outside the critical region. Hence, these isotherms do not lie on the upper scaling curve ϵ_+, and moreover, on a log-log data collapse they appear as a straight line with zero slope. With decreasing temperature the rescaled resistivity, $y=\rho/|\vartheta|^{\mu}$ develops an Ohmic component at low rescaled current densities, $x=J/|\vartheta|^{\lambda}$, a power-law component at intermediate rescaled current densities, and an Ohmic region at sufficiently high rescaled current densities. Both the Ohmic and the power-law regions lie within the critical region and thus collapse on to the upper scaling curve ϵ_+.

Moreover, since $\epsilon_+(x\rightarrow0)\sim x$, the corresponding linear resistivity regions appear as a straight line with zero slope on a log-log data collapse. Deviations from ϵ_+ at sufficiently

TABLE III. Summary of available field-dependent I-V data taken for each of the six samples.

H	$S1$	$S4$	$S7$	$S9$	$S15$	SB
0.5 G	×			×	×	
30 G	×		×	×	×	
100 G	×		×	×	×	×
200 G	×	×				
500 G	×	×	×	×	×	×
1 kG					×	×
2 kG				×	×	
3 kG			×		×	
4 kG			×	×	×	
5 kG		×				
1 T			×	×	×	×
5 T					×	×
10 T			×	×		

high rescaled current densities correspond to the portions of the isotherms that lie outside the critical region. Close to the transition the rescaled data exhibit a power-law character (upper right section of the data collapses) consistent with the expected form $\epsilon_{\pm}(x\rightarrow\infty)\sim x^{a}$. Below the transition, portions of the rescaled data lie on the lower scaling form ϵ_{-}. The negative curvature of ϵ_{-} is consistent with the superconducting response of the sample at these temperatures. The shape of the lower scaling form is consistent with, but does not uniquely imply the predicted glassy response $\epsilon_{-}(x\rightarrow 0)\sim\exp(-a/x^{s})$. The glass exponent s is hard to measure due to the limited dynamic range and low density of data points. Finally, deviations from ϵ_{-} correspond to the high rescaled current density portion of the isotherms that lie outside the critical region. The optimum data collapse was found using the T_c found from the E-J curves and using various combinations of μ and λ. The quality of the data collapse was determined using the following criteria in order of decreasing importance: scaling of the linear resistivities,

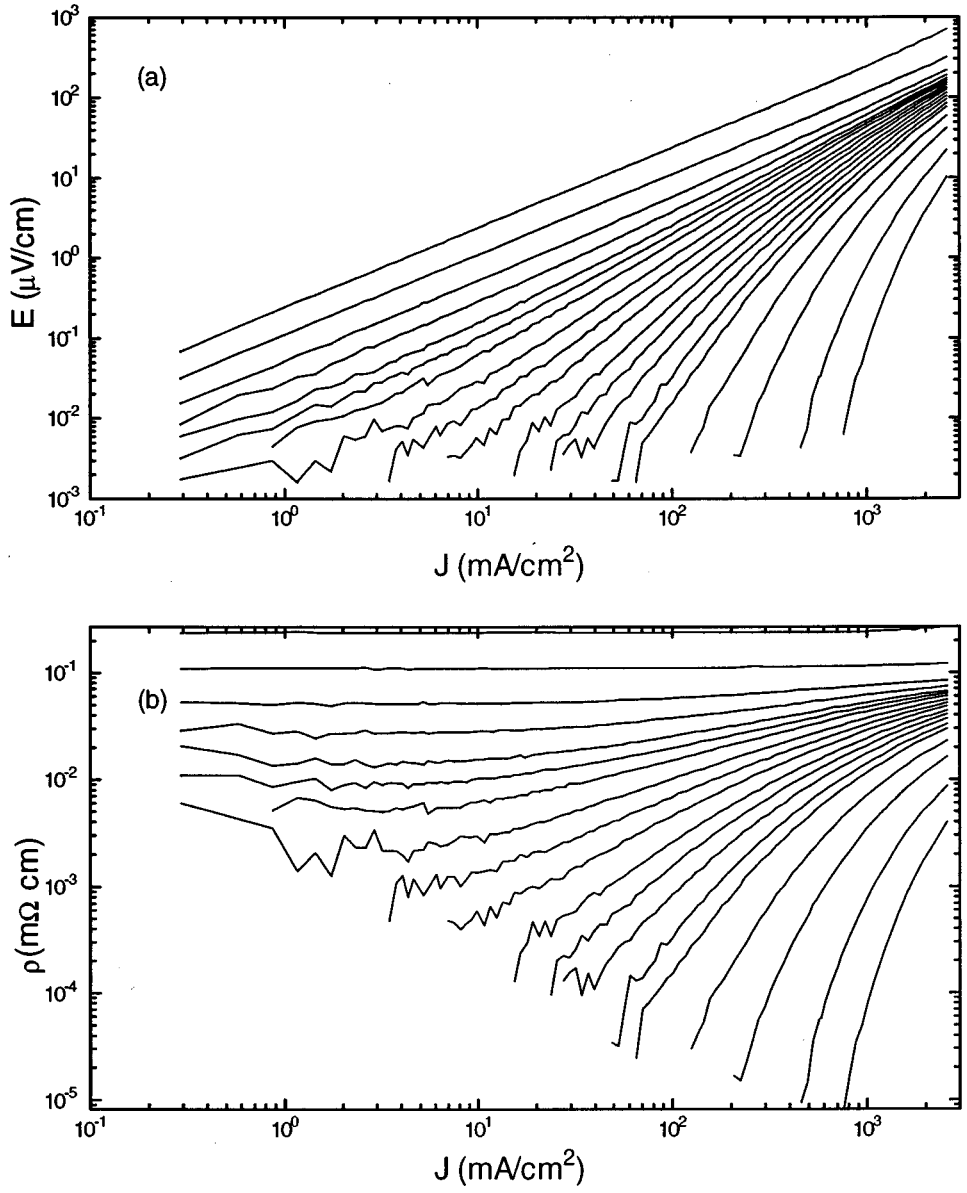

FIG. 6. (a) Selected E-J isotherms for sample $S15$ at $H=100$ G. (b) The same data plotted as resistivity, E/J, vs J.

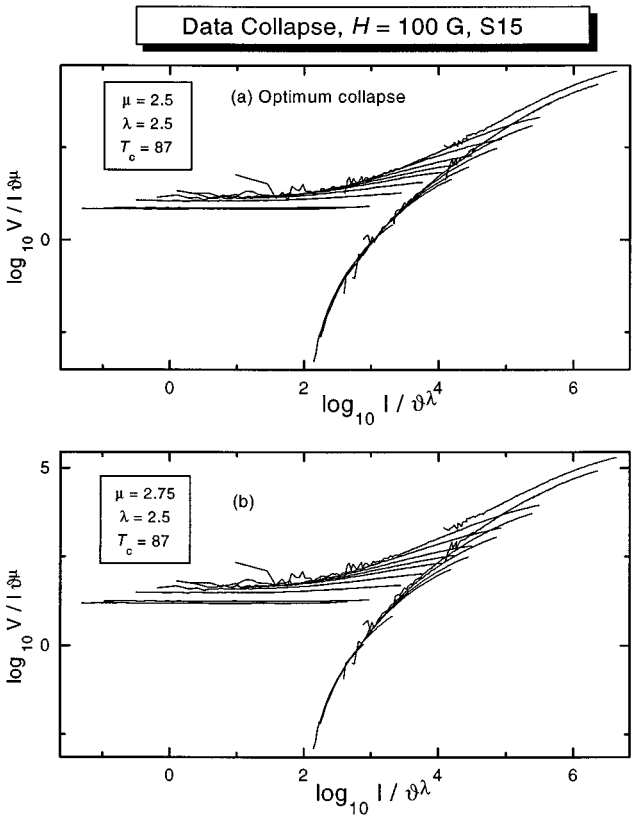

FIG. 7. Data collapses for sample $S15$ at $H=100$ G. (a) Optimum data collapse. (b) Data collapse with different μ showing systematic deviations from the scaling curves.

scaling of isotherms close to T_c and scaling of the isotherms below T_c. The parameters of the optimum collapse were those that produced optimum scaling in all three regions. The precision in T_c, μ, and λ were determined by fixing two of the parameters and adjusting the third until subsequent changes in that parameter produced systematic deviations from the optimum collapse. Figure 7 shows the data collapse for sample S15 at $H=100$ G when the value of μ was changed from its optimum value, $\mu=2.5$ to $\mu=2.75$. Systematic deviations for the isotherms close to T_c are clearly visible along with small deviations for the linear resistivities and the lower scaling curve ϵ_-.

Above the transition there is a crossover from power-law behavior to Ohmic behavior below a temperature-dependent current density J_x^+. In the linear region $E=\rho_L J$ or

$$\ln E=\ln\rho_L+\ln J. \tag{26}$$

We picked the upper limit of the Ohmic region to correspond to the value of J above which the slopes showed systematic monotonic increases over unity. Using that value for the upper limit of the Ohmic region we extracted the resistivity from the intercept from the $\ln E$ vs $\ln J$ plot. Figure 8 shows the E-J data for the sample S15 at $H=100$ G. The points represent the E-J data with error bars corresponding to $1\sigma\sim1$ nV/cm statistical uncertainty. The straight lines correspond to the low-J linear fits to the data. These figures clearly show the crossover from Ohmic to power-law behavior. They also show the vanishing of linear resistivity (decreasing slope) and the reduction in the size of the Ohmic region as the transition is approached. Figure 8(c) shows ρ_L vs ϑ and shows the characteristic vanishing of resistivity as the transition is approached ($\vartheta\rightarrow0$). The scaling relationship predicts power-law behavior in the linear resistivity ρ_L with respect to the reduced temperature ϑ. Thus, when plotted as $\ln\rho_L$ vs $\ln\vartheta$ all the data in the scaling region should lie on a straight line with slope μ. This aspect of the analysis also serves as a consistency check on the exponent μ extracted previously from the data collapse. The dynamic range of power-law behavior seems to extend over a maximum of two decades in resistivity from $\rho_L\sim100$ $\mu\Omega$ cm to $\rho_L\sim1$ $\mu\Omega$ cm. At higher temperatures the linear resistivities lie outside the critical region and thus show deviations from power-law behavior. The E-J isotherms corresponding to these points do not appear to collapse on to the upper scaling curve ϵ_+. For example from the optimum data collapse for sample S15 at $H=100$ G we see that the first three E-J isotherms do not appear to collapse onto ϵ_+. Similarly, from Fig. 8(b) the resistivities corresponding to the first two isotherms appear to deviate from power-law behavior. Deviations close to T_c, on the other hand, are not indicative of data outside of the critical region but instead reflect the limits on our experimental window. This lower limit corresponded to $\rho_L\sim1$ $\mu\Omega$ cm and we did not include any points below this limit in our fits. The critical exponent μ was extracted by performing weighted fits to the data in the power-law region. We used mean values of T_c and δT_c from the data collapse and the E-J isotherms, respectively, for the power-law fits. Based on the above technique our results were consistent with $\mu=2.3\pm0.2$ for sample S15 at $H=100$ G.

Using the procedures described above we were able to extract the critical temperature T_c and the critical exponents a, μ, λ, ν, and z for each sample and field. The average values of the parameters obtained from the various tests are summarized in Tables IV–IX. Thus

$$\langle a\rangle=(a_{\mathrm{IV}}+a_{\mathrm{DC}})/2, \tag{27}$$

$$\langle\mu\rangle=(\mu_{\mathrm{DC}}+\mu_{\mathrm{LR}})/2, \tag{28}$$

$$\langle\lambda\rangle=\lambda_{\mathrm{DC}}, \tag{29}$$

$$\langle\nu\rangle=\nu_{\mathrm{DC}}, \tag{30}$$

$$\langle z\rangle=(z_{\mathrm{IV}}+z_{\mathrm{DC}})/2, \tag{31}$$

where the subscripts IV, DC, and LR refer to the IV, data collapse, and linear resistivity tests, respectively.

Figure 9 shows ν and z vs H for all the samples. Our experimental results can be compared with the theoretical predictions of the glass models. For a d-dimensional glass system with an m component order parameter the corresponding static exponent, ν can be expressed as[4]

$$\nu=1/2+5(6-d)/24 \quad \text{(gauge glass)}, \tag{32}$$

$$\nu=1/2+5md/12(2m-1) \quad \text{(spin glass)}. \tag{33}$$

For spin systems the corresponding expression is[4]

$$\nu=1/2+(m+2)(4-d)/4(n+8) \quad \text{(spin models)}. \tag{34}$$

These expressions are evaluated for the various systems in Table X below.

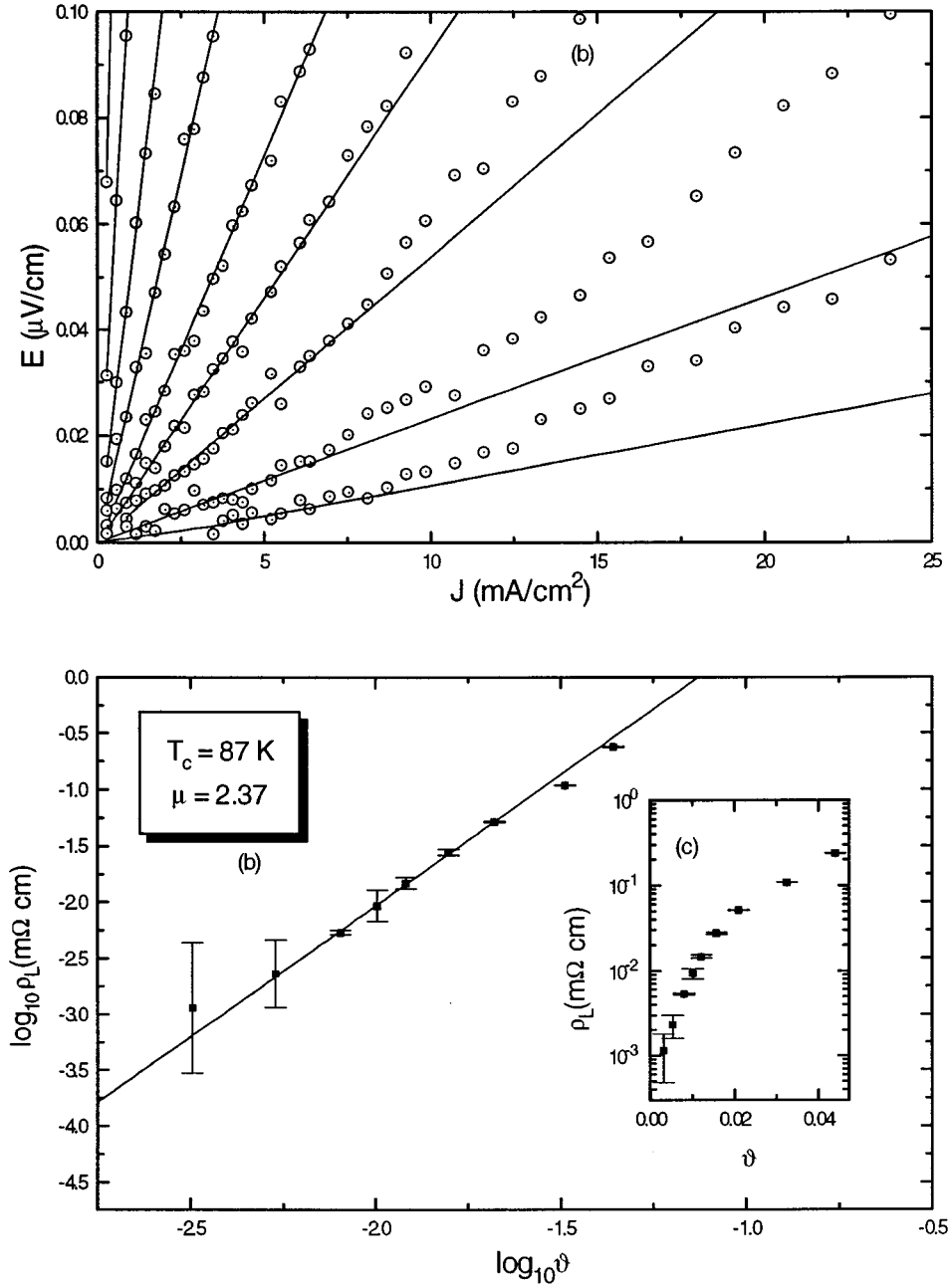

FIG. 8. Data analysis plots for sample $S15$ at $H=100$ G. (a) ρ_L fits for selected E-J isotherms above T_c. (b) $\ln\rho_L$ vs $\ln\vartheta$. (c) ρ_L vs ϑ.

From the table we see that the theoretical prediction for a 3D gauge glass is $\nu=1.13$. This result holds for all fields above the glass field, H_g and is morphology independent. The glass field is given by $H_g \sim \phi_0/2\xi_p^2$, where ξ_p is the percolation coherence length. For a granular sample $\xi_p \sim \langle d_g \rangle$, the average grain size in the sample. For a granular sample with $\langle d_g \rangle \sim 1$ μm $H_g \sim 1$ G. Since our samples had $\langle d_g \rangle \geqslant 1$ μm and the minimum applied magnetic field was 0.5

TABLE IV. Summary of critical exponents $\langle a \rangle$, $\langle \mu \rangle$, $\langle \lambda \rangle$, $\langle \nu \rangle$, and $\langle z \rangle$ and critical temperature, T_c for sample SB in selected magnetic fields, H.

H	T_c (K)	$\langle a \rangle$	$\langle \mu \rangle$	$\langle \lambda \rangle$	$\langle \nu \rangle$	$\langle z \rangle$
100 G	85.9±0.15	2.3±0.24	3.5±0.35	2.5±0.3	1.25±0.15	3.62±0.34
500 G	82.6±0.15	2.32±0.22	3.1±0.2	2.35±0.3	1.17±0.15	3.65±0.33
1 kG	80.8±0.2	2.2±0.2	2.75±0.2	2.3±0.1	1.15±0.05	3.4±0.33
1 T	78.75±0.25	1.85±0.3	2±0.35	2.5±0.25	1.25±0.13	2.7±0.4
5 T	72.1±0.5	1.8±0.25	1.9±0.4	2.5±0.25	1.25±0.13	2.6±0.3

TABLE V. Summary of critical exponents $\langle a\rangle$, $\langle\mu\rangle$, $\langle\lambda\rangle$, $\langle\nu\rangle$, and $\langle z\rangle$ and critical temperature, T_c for sample $S1$ in selected magnetic fields, H.

H	T_c (K)	$\langle a\rangle$	$\langle\mu\rangle$	$\langle\lambda\rangle$	$\langle\nu\rangle$	$\langle z\rangle$
0.5 G	90.75±0.11	2.65±0.55	3.9±0.75	2.2±0.2	1.1±0.1	4.32±0.8
30 G	89.1±0.2	2.66±0.35	4.33±0.65	2.5±0.2	1.25±0.1	4.32±0.525
100 G	87.22±0.2	2.43±0.35	3.63±0.5	2.5±0.3	1.25±0.15	3.86±0.5
200 G	85.45±0.2	2.54±0.28	3.6±0.4	2.2±0.2	1.1±0.1	4.1±0.38
500 G	82.6±0.4	2.7±0.53	3.9±0.8	2.3±0.3	1.15±0.15	4.38±0.73

TABLE VI. Summary of critical exponents $\langle a\rangle$, $\langle\mu\rangle$, $\langle\lambda\rangle$, $\langle\nu\rangle$, and $\langle z\rangle$ and critical temperature, T_c for example $S4$ in selected magnetic fields, H.

H	T_c (K)	$\langle a\rangle$	$\langle\mu\rangle$	$\langle\lambda\rangle$	$\langle\nu\rangle$	$\langle z\rangle$
200 G	87.9±0.1	1.89±0.17	2.13±0.38	2.5±0.2	1.25±0.1	2.7±0.23
500 G	85.9±0.1	2.1±0.2	2.47±0.25	2.25±0.25	1.13±0.13	3.22±0.27
5 kG	82.2±0.4	2±0.25	2.35±0.33	2.25±0.25	1.13±0.13	3.1±0.38

TABLE VII. Summary of critical exponents $\langle a\rangle$, $\langle\mu\rangle$, $\langle\lambda\rangle$, $\langle\nu\rangle$, and $\langle z\rangle$ and critical temperature, T_c for sample $S7$ in selected magnetic fields, H.

H	T_c (K)	$\langle a\rangle$	$\langle\mu\rangle$	$\langle\lambda\rangle$	$\langle\nu\rangle$	$\langle z\rangle$
30 G	88±0.1	2±0.3	3.1±0.45	3.5±0.25	1.75± 0.25	3± 0.35
100 G	85.9±0.3	2.2±0.3	3±0.55	2.5±0.5	1.25± 0.25	3.4± 0.36
500 G	85.4±0.3	2±0.35	2.9±0.55	3±0.5	1.5± 0.25	3± 0.45
3 kG	82.46±0.3	2.1±0.24	2.9±0.5	2.75±0.25	1.38±0.13	3.15±0.33
1 T	80±0.3	1.95±0.2	3±0.3	2.5±0.25	1.5±0.13	2.9±0.3
10 T	73.2±1	1.9±0.3	3±0.35	3±0.5	1.5±0.25	2.75±0.35

TABLE VIII. Summary of critical exponents $\langle a\rangle$, $\langle\mu\rangle$, $\langle\lambda\rangle$, $\langle\nu\rangle$, and $\langle z\rangle$ and critical temperature, T_c for sample $S9$ in selected magnetic fields, H.

H	T_c (K)	$\langle a\rangle$	$\langle\mu\rangle$	$\langle\lambda\rangle$	$\langle\nu\rangle$	$\langle z\rangle$
0.5 G	90.45±0.15	1.67±0.25	1.62±0.2	2.5±0.2	1.25±0.1	2.34±0.42
30 G	89.4±0.1	1.75±0.2	1.7±0.2	2.4±0.1	1.2±0.05	2.5±0.3
100 G	88.9±0.1	1.85±0.2	1.9±0.2	2.1±0.2	1.1±0.1	2.7±0.3
500 G	88±0.1	1.83±0.2	1.8±0.2	2.2±0.1	1.1±0.1	2.7±0.25
2 kG	86.3±0.2	2.1±0.3	2.1±0.35	2.2±0.2	1.1±0.1	3.2±0.45
4 kG	85.5±0.15	2±0.25	2.13±0.25	2.25±0.25	1.13±0.13	3±0.3
1 T	84.5±0.2	1.94±0.25	2.25±0.25	2.5±0.25	1.13±0.13	2.9±0.4
10 T	78.6±0.25	2±0.3	2.35±0.3	2.25±0.25	1.13±0.13	3.1±0.45

TABLE IX. Summary of critical exponents $\langle a\rangle$, $\langle\mu\rangle$, $\langle\lambda\rangle$, $\langle\nu\rangle$, and $\langle z\rangle$ and critical temperature, T_c for sample $S15$ in selected magnetic fields, H.

H	T_c (K)	$\langle a\rangle$	$\langle\mu\rangle$	$\langle\lambda\rangle$	$\langle\nu\rangle$	$\langle z\rangle$
0.5 G	89.62±0.05	1.9±0.15	2.43±0.2	3±0.1	1.5±0.13	2.75±0.2
30 G	87.9±0.1	1.92±0.15	2.25±0.25	2.5±0.15	1.25±0.13	2.85±0.2
100 G	87±0.1	2.1±0.2	2.42±0.2	2.5±0.25	1.25±0.13	3.1±0.3
500 G	85.7±0.2	2±0.33	2.4±0.3	2.5±0.25	1.25±0.13	3±0.5
1 kG	85±0.25	2±0.25	2.2±0.3	2.25±0.25	1.13±0.13	3±0.4
2 kG	83.7±0.25	2.15±0.25	2.7±0.3	2.5±0.25	1.25±0.13	3.3±0.33
3 kG	82.75±0.25	2.35±0.22	3.35±0.3	2.5±0.25	1.25±0.13	3.7±0.3
4 kG	81.85±0.15	2.5±0.2	3.7±0.25	2.5±0.25	1.25±0.13	4±0.25
1 T	81.15±0.35	2.05±0.38	2.9±0.5	2.5±0.5	1.25±0.13	3.1±0.5
5 T	77.2±0.35	2.15±0.4	3.05±0.35	2.5±0.5	1.25±0.13	3.3±0.5

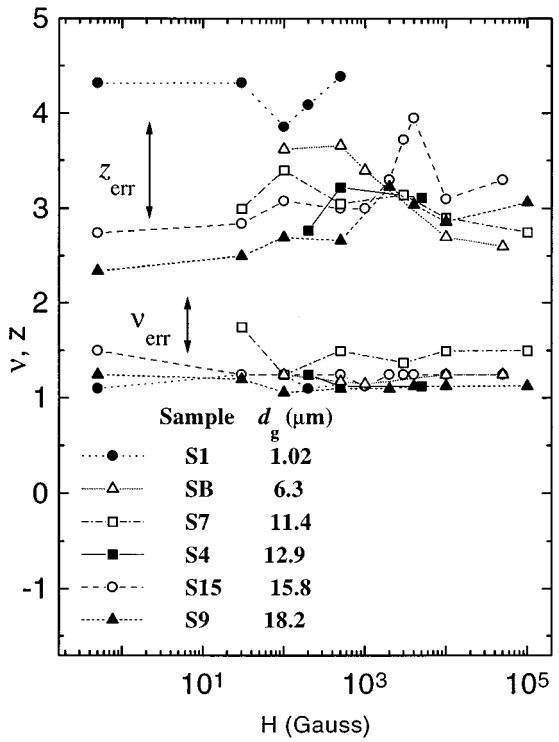

FIG. 9. ν and z vs H for all six samples.

G, it follows that all our measurements were taken above H_g. From the ν vs H plots we see that the theoretical value of ν does lie within the range of precision set on the corresponding experimentally measured value of ν. Furthermore the static exponent does not seem to display any field or morphology dependence (Fig. 9). Thus our measurements of ν are consistent with the 3D granular gauge glass model.

The dynamic exponent, z is harder to calculate theoretically. For a 3D spin glass the prediction is that $z>4$. Monte Carlo simulations of the I-V characteristics based on the gauge glass model predict $z\sim2$. This value is close to the mean-field prediction where $z\sim2.2$. Thus it is likely that the simulations do not probe the critical region. Our measurements of z show two characteristic features: some morphology dependence, and $z<4$ for most samples and fields. Our z values are comparable to those measured earlier by Tiernan, Joshi, and Hallock.[7] Their samples were fabricated by completely different processing method, the polymer precursor technique. Our z measurements are in disagreement with those obtained on granular YBCO samples by Worthington *et al.*[8] Our measurement technique was identical to that used by Tiernan, Joshi, and Hallock[7] and Worthington *et al.*[8] Thus the similarity of our z values with those obtained by Tiernan, Joshi, and Hallock[7] establishes the independence of these results with respect to sample fabrication technique.

TABLE X. Critical exponents for various superconducting and spin systems.

System	d	m	ν	z
Spin glass	3	2	1.33	>4
	3	3	1.25	>4
Gauge glass	3	2	1.13	>4
Mean field	3	2	0.5	2.2
XY spins	3	2	0.67	

Morphology and field dependence of the dynamic exponent z is illustrated in Fig. 9. From the figure we see that the small grain-size samples, $S1$ and SB display somewhat higher z values in low to intermediate fields than the z values of the other larger grain-size samples, $S4$, $S7$, $S9$, and $S15$. Moreover, one of the samples, $S15$ displays interesting systematic evolution in z values from $z\sim2.7$ in low fields to $z\sim4$ in intermediate magnetic fields. Sample $S7$ also seems to display some evolution in z as a function of increasing field up to intermediate fields. The evolution in z values is also reflected in the corresponding experimental exponent, μ. Samples $S4$ and $S9$, however, do not show any trends in the dynamic exponent. All the high-field data taken on samples SB, $S7$, $S9$, and $S15$ do not display a continuation in the trends displayed in their low-field counterparts. All the high-field z values were in the range $z\sim2.5$–3.2. There are several possible explanations for this behavior. One possibility is the reduction of our experimental window for viewing the critical region. This makes estimation of the critical isotherm and hence the z value much harder. Moreover the quality of the high-field data collapses was not as good as that obtained for the low- to intermediate-field data. Another related possibility for the low z values in high fields is that our measurements probe the transition region between the critical region and the mean-field domain. This would account for the lower, nearly mean-field-like behavior of z. One final possibility is that the measurements are reflective of the critical region in a granular superconductor for high fields.

We have noted earlier that our z values are in gross disagreement with the prediction for the glassy models. Does this mean that our data does not probe the critical region? That may well be a possible explanation for the poor quality of the data collapses in high fields. For the low-field data however we obtained excellent data collapses and reasonably good agreement from the consistency checks. Moreover the static exponent was in good agreement with the 3D gauge glass prediction and significantly greater than the mean-field

TABLE XI. Summary of critical exponents for various YBCO systems.

System	Field, H	Group	ν	z
Bulk granular	0.5 G–10 T	This study	1.1–1.75	2.3–4.3
	0.5 G–81 G	Tiernan *et al.* (Ref. 7)	1.3–1.6	2.6–3.4
	500 G–1.5 T	Worthington *et al.* (Ref. 8)	1.1±0.2	4.6±0.2
Single crystal	1.5–6 T	Gammel *et al.* (Ref. 18)	2±1	4.3±1.5
Thin film	0.5–4 T	Koch *et al.* (Ref. 12)	1.7±0.2	4.8

value. Thus we believe that our low- to intermediate-field z values are truly reflective of the underlying dynamics of the granular superconducting system in the context of the scaling predictions and the gauge glass model. The comparison of our results with the results obtained by various other groups on various YBCO systems is shown in Table XI.

CONCLUSION

We have studied the I-V characteristics of six granular samples of YBCO with varying morphologies and over the entire accessible field range. This distinguishes our work from previous studies that were restricted to specific field ranges and in samples of fairly small grain sizes. Our studies addressed issues related to superconducting systems and to the more general area of phase transitions and dynamic phenomena. The complex nonlinear evolution of the I-V characteristics within the critical region is consistent with the scaling hypothesis of Fisher, Fisher, and Huse. Furthermore the value of the static exponent, ν is consistent with the 3D gauge glass model. Our values for the dynamic exponent, z are significantly lower than the values predicted by analogy with the spin-glass systems. z shows some morphology dependence and for some of the samples z also displays evolution in field.

ACKNOWLEDGMENTS

We thank W. Tiernan for discussions and J.S. Brooks and the staff of the NHMFL for insistance in expediting the measurements. This work was supported by UMASS Research Trust Funds, and the NSF through MRSEC DMR 94-00488, by NSF DMR 91-22348, 94-22208, and by NHMFL via NSF DMR 90-16241.

[1] M. Tinkham and C. J. Lobb, in *Solid State Physics: Advances and Applications*, edited by H. Erenreich and D. Turnbull (Academic, New York, 1989), Vol. 42, p. 91.
[2] M. A. Dubson, S. T. Hebart, J. J. Calabrese, D. C. Harris, B. R. Patton, and J. C. Garland, Phys. Rev. Lett. **60**, 1061 (1988).
[3] W. Y. Shih, C. Ebner, and D. Stroud, Phys. Rev. B **30**, 134 (1984).
[4] A. Houghton and M. A. Moore, Phys. Rev. B **38**, 5045 (1988).
[5] D. S. Fisher, M. P. A. Fisher, and D. A. Huse, Phys. Rev. B **43**, 130 (1991).
[6] M. P. A. Fisher, Phys. Rev. Lett. **62**, 1415 (1989).
[7] W. M. Tiernan, R. Joshi, and R. B. Hallock, Phys. Rev. B **48**, 3423 (1993).
[8] T. K. Worthington, E. Olsson, C. S. Nichols, T. M. Shaw, and D. R. Clarke, Phys. Rev. B **43**, 10 538 (1991).
[9] M. Tinkham, *Introduction to Superconductivity*, 2nd ed. (McGraw-Hill, New York, 1996), p. 201.
[10] V. Ambegaokar and A. Baratoff, Phys. Rev. Lett. **10**, 486 (1963).
[11] V. Ambegaokar and B. I. Halperin, Phys. Rev. Lett. **22**, 1364 (1969).
[12] R. H. Koch, V. Foglietti, W. J. Gallagher, G. Koren, A. Gupta, and M. P. A. Fisher, Phys. Rev. Lett. **63**, 1511 (1989).
[13] C. Dekker, W. Eidelloth, and R. Koch, Phys. Rev. Lett. **68**, 3347 (1992).
[14] J. W. Ekin, A. J. Panson, and B. A. Blankenship, Appl. Phys. Lett. **52**, 331 (1988).
[15] J. W. Ekin, T. M. Larson, N. F. Bergren, A. J. Nelson, A. B. Swartzlander, L. L. Kazmerski, A. J. Panson, and B. A. Blankenship, Appl. Phys. Lett. **52**, 1819 (1988).
[16] A. M. M. Barus and J. A. T. Taylor, Physica C **225**, 374 (1994).
[17] Seattle Specialty Ceramics, Ceramic Powder Synthesis and Processing, Woodinville, WA, 98072.
[18] P. L. Gammel, L. F. Schneemeyer, and D. J. Bishop, Phys. Rev. Lett. **66**, 953 (1991).